

Spatio-Temporal Scintillation Mitigation via Polarizations Coupled Higher-Order Correlation

Shouvik Sadhukhan^{1,*} and C. S. Narayanamurthy²

^{1,2}Applied and Adaptive Optics Laboratory, Department of Physics, Indian Institute of Space Science and Technology (IIST), P.O: Valiamala, Trivandrum - 695547, State: Kerala; India

¹Email: shouvikphysics1996@gmail.com

²Email: naamu.s@gmail.com

*Corresponding Author Email: shouvikphysics1996@gmail.com

March 10, 2026

Abstract

We present a unified theoretical framework that links the second- and fourth-order statistical correlation properties of stochastic electromagnetic beams to the scintillation index observed after propagation through Kolmogorov atmospheric turbulence. We derived the beam coherence-polarisation (BCP) matrix and its propagation law through a random medium. The algebraic bridge has been established between the second-order polarization matrix \mathbf{J} , its Gram (fourth-order) counterpart $\mathbf{\Omega} = \mathbf{J}^2$, the classical degree of polarization P , the fourth-order degree of polarization P_Ω , and the scintillation index σ_I^2 . A key result is the closed-form purity relation $\text{Tr}(\mathbf{J}^2)/(\text{Tr} \mathbf{J})^2 = (1 + P^2)/2$, from which it follows directly that unpolarised (natural) beams exhibit large scintillation index which can be reduced by polarizing the beams with the use of polariser sets. The reduction holds independently of the turbulence strength parameter, C_n^2 . Experimental results demonstrate that simultaneous control of coherence and polarization—achievable experimentally with a Pseudo Random Phase Plate (PRPP)—offers a practical route to minimizing scintillation in free-space optical communication links.

Keywords: Lorentz Dipole Oscillation, Kolmogorov Statistics, Scintillation Index, Pseudo Random Phase Plate (PRPP), Polarization Matrix, Fourth-Order Correlations

1 Introduction

The reliable transmission of optical signals through the turbulent atmosphere remains a central challenge in free-space optical (FSO) communications and remote sensing. Refractive-index fluctuations induced by thermal convection follow, to an excellent approximation, Kolmogorov statistics [5], and they impose random amplitude and phase modulation on any propagating wave. The resulting intensity fluctuations at the receiver—quantified by the scintillation index σ_I^2 —degrade the signal-to-noise ratio and can cause link outages.

Two complementary strategies are widely employed to mitigate scintillation. The first exploits *receiver aperture averaging*: when the collecting aperture exceeds the transverse coherence radius of the intensity pattern, the fluctuations in collected power are suppressed [62]. The second, known as *transmitter aperture averaging* or source-diversity, relies on partially coherent illumination: it has been shown both analytically and experimentally that reducing the spatial coherence of the transmitter reduces the on-axis scintillation index, at least in the weak-fluctuation regime [2, 5].

What has received considerably less attention is the role of the *polarization state* of the source in governing the intensity fluctuations. Korotkova [2, 5] showed, within the framework of electromagnetic beam theory, that an unpolarized (natural) beam and a fully linearly polarized beam can share identical intensity profiles and identical degrees of coherence yet exhibit scintillation indexes differing by exactly a factor of two—the unpolarized beam being the quieter one. This result is remarkable in that it is *independent* of the statistical properties of the medium: it holds for any homogeneous isotropic turbulence, at any strength, as a direct consequence of the algebraic structure of the fourth-order correlation matrix.

The microscopic origin of this sensitivity to polarization can be traced to the oscillator model of the source. A Lorentz dipole oscillator with a nonlinear (anharmonic) restoring force [23, 28, 29] generates radiation whose statistical properties—and in particular whose higher-order moments—are richer than those of a harmonic oscillator. When two such oscillators are driven along orthogonal polarization axes with mutually independent fluctuating amplitudes (the “natural light” condition), the cross-correlation of their intensities vanishes and the total scintillation index is halved relative to the single-polarization case. This suppression mechanism is fundamentally different from coherence-based suppression and is operative in all turbulence regimes.

The present paper has three objectives. First, we provide a self-contained derivation of the polarization matrix \mathbf{J} , its eigenvalue decomposition, the degree of polarization P , and the Gram matrix $\mathbf{\Omega} = \mathbf{J}^2$, making explicit the purity relation that connects second-order and fourth-order statistics. Second, we re-derive the scintillation index of an electromagnetic beam propagating through Kolmogorov turbulence within the unified framework, clarifying how P and the fourth-order degree of polarization P_{Ω} enter the final result. Third, we demonstrate via experiment with gaussian beams that the combined optimization of coherence and polarization—implemented in practice through a Pseudo Random Phase Plate (PRPP)—yields the lowest attainable scintillation index at any propagation distance and any turbulence strength.

The remainder of the paper is organized as follows. Section 2 develops the theoretical framework, including the BCP matrix, its propagation law, the eigenvalue decomposition, and the derivation of the scintillation index. Section 3 describes the experimental implementation using a PRPP. Section 4 discusses the results, and Section 5 summarizes the main findings.

2 Theoretical Framework

2.1 Second-Order Correlation Matrix and Polarization

Consider a wide-sense statistically stationary, quasi-monochromatic electromagnetic beam propagating close to the z -axis. At any transverse position $\boldsymbol{\rho}$ in the plane $z = \text{const}$, the electric field has two mutually orthogonal Cartesian components $E_x(\boldsymbol{\rho}, z, t)$ and $E_y(\boldsymbol{\rho}, z, t)$. The second-order statistical properties at a single point are encoded in the 2×2 polarization (coherency) matrix [2, 5]

$$J_{\alpha\beta} = \langle E_{\alpha}^*(\boldsymbol{\rho}, z, t) E_{\beta}(\boldsymbol{\rho}, z, t) \rangle, \quad \alpha, \beta \in \{x, y\}, \quad (1)$$

which in explicit form reads

$$\mathbf{J} = \begin{pmatrix} \langle |E_x|^2 \rangle & \langle E_x^* E_y \rangle \\ \langle E_y^* E_x \rangle & \langle |E_y|^2 \rangle \end{pmatrix}. \quad (2)$$

The matrix \mathbf{J} is Hermitian and positive semi-definite. Its trace gives the average intensity,

$$I = \text{Tr } \mathbf{J} = \langle |E_x|^2 \rangle + \langle |E_y|^2 \rangle, \quad (3)$$

while its determinant is $\det \mathbf{J} = \langle |E_x|^2 \rangle \langle |E_y|^2 \rangle - |\langle E_x^* E_y \rangle|^2$.

2.1.1 Eigenvalue Decomposition

Since \mathbf{J} is Hermitian it can be unitarily diagonalized,

$$\mathbf{J} = \mathbf{U} \begin{pmatrix} \lambda_1 & 0 \\ 0 & \lambda_2 \end{pmatrix} \mathbf{U}^{\dagger}, \quad \lambda_1 \geq \lambda_2 \geq 0, \quad (4)$$

with matrix invariants

$$\text{Tr } \mathbf{J} = \lambda_1 + \lambda_2, \quad \det \mathbf{J} = \lambda_1 \lambda_2. \quad (5)$$

2.1.2 Degree of Polarization

The classical degree of polarization is defined as [2, 5]

$$P = \sqrt{1 - \frac{4 \det \mathbf{J}}{(\text{Tr } \mathbf{J})^2}}, \quad (6)$$

which in terms of eigenvalues reads

$$P = \frac{|\lambda_1 - \lambda_2|}{\lambda_1 + \lambda_2}. \quad (7)$$

Thus $P = 1$ for fully polarized light ($\lambda_2 = 0$) and $P = 0$ for natural (unpolarized) light ($\lambda_1 = \lambda_2$).

2.2 Fourth-Order Correlation Matrix and Gram Matrix

The fourth-order statistical properties of the field at a single point are described by the 4×4 matrix [2, 5]

$$\Gamma_{\alpha\beta\gamma\delta}^{(2,2)} = \langle E_\alpha^* E_\beta E_\gamma^* E_\delta \rangle, \quad \alpha, \beta, \gamma, \delta \in \{x, y\}. \quad (8)$$

For fields obeying complex circular Gaussian statistics the moment theorem [2] gives

$$\langle E_\alpha^* E_\beta E_\gamma^* E_\delta \rangle = \langle E_\alpha^* E_\beta \rangle \langle E_\gamma^* E_\delta \rangle + \langle E_\alpha^* E_\delta \rangle \langle E_\gamma^* E_\beta \rangle, \quad (9)$$

which allows all fourth-order moments to be expressed in terms of second-order ones.

The *Gram matrix* $\mathbf{\Omega}$ is defined as

$$\mathbf{\Omega} = \mathbf{J}^\dagger \mathbf{J}. \quad (10)$$

Since \mathbf{J} is Hermitian, $\mathbf{J}^\dagger = \mathbf{J}$ and therefore

$$\mathbf{\Omega} = \mathbf{J}^2. \quad (11)$$

Its trace is

$$\text{Tr}(\mathbf{\Omega}) = \text{Tr}(\mathbf{J}^2) = \lambda_1^2 + \lambda_2^2. \quad (12)$$

Explicitly, using (9),

$$\text{Tr}(\mathbf{\Omega}) = \langle |E_x|^2 \rangle^2 + \langle |E_y|^2 \rangle^2 + 2|\langle E_x^* E_y \rangle|^2. \quad (13)$$

2.2.1 Purity Relation

From equations (6)–(12) a fundamental algebraic identity follows:

$$\frac{\text{Tr}(\mathbf{J}^2)}{(\text{Tr} \mathbf{J})^2} = \frac{\lambda_1^2 + \lambda_2^2}{(\lambda_1 + \lambda_2)^2} = \frac{1 + P^2}{2}. \quad (14)$$

Equation (14) is the central *purity relation* that bridges second-order polarization statistics and the Gram trace entering the scintillation index.

2.2.2 Fourth-Order Degree of Polarization

Analogously to (6) one defines, for the Gram matrix with eigenvalues $\lambda_1^2 \geq \lambda_2^2$,

$$P_\Omega = \sqrt{1 - \frac{4 \det \mathbf{\Omega}}{(\text{Tr} \mathbf{\Omega})^2}} = \frac{\lambda_1^2 - \lambda_2^2}{\lambda_1^2 + \lambda_2^2}. \quad (15)$$

Using (7) one finds the closed-form relation

$$P_\Omega = \frac{2P}{1 + P^2}, \quad (16)$$

and equations (14) and (16) together give

$$\frac{\text{Tr}(\mathbf{\Omega})}{(\text{Tr} \mathbf{J})^2} = \frac{1 + P^2}{2} = \frac{1 + P_\Omega}{2} \cdot \frac{1 + P^2}{1 + P_\Omega}. \quad (17)$$

The complete unified relation between second- and fourth-order quantities is therefore

$$\frac{\text{Tr}(\mathbf{\Omega})}{(\text{Tr} \mathbf{J})^2} - 1 = \frac{P^2 - 1}{2} = \frac{P_\Omega - 1}{1 + P^2/(P_\Omega \cdot \dots)}. \quad (18)$$

In the practically important limiting cases:

- Fully polarized ($P = 1$): $\text{Tr}(\mathbf{J}^2)/(\text{Tr} \mathbf{J})^2 = 1$.
- Unpolarized ($P = 0$): $\text{Tr}(\mathbf{J}^2)/(\text{Tr} \mathbf{J})^2 = 1/2$.

3 Experimental setup

3.1 Optical System Configuration

The experimental apparatus is illustrated in Figure 1. A continuous-wave He-Ne laser operating at $\lambda = 632.8$ nm served as the coherent light source. The output beam was spatially filtered and collimated using a spatial filter assembly (SFA) consisting of a microscope objective, a pinhole, and a collimating lens, yielding a clean, diffraction-limited Gaussian beam of approximately 5 mm diameter ($1/e^2$). The collimated beam was directed onto a Pseudo-Random Phase Plate (PRPP, Thorlabs EDU-RPP1) mounted on a motorized rotation stage, which introduced controlled Kolmogorov-type wavefront aberrations to simulate atmospheric turbulence (Section 3.2). After passing through the PRPP, the turbulence-impacted beam propagated through a set of thin-film linear polarizers (0–5 polarizers, depending on the experimental set) placed in series along the optical axis. The transmitted beam was then imaged onto a CCD camera (Thorlabs DCC1545M) using an imaging lens, and the recorded intensity distributions were stored for offline analysis.

The polarizers were identical high-extinction-ratio thin-film linear polarizers, each with its transmission axis aligned along the same orientation so that successive polarizers acted cumulatively to enforce a higher degree of linear polarization and reduce the effective beam volume presented to the detection plane. No additional adaptive-optics or wavefront-correction elements were employed, making the system a purely passive scintillation-mitigation configuration. The turbulence-free reference dataset (Set 7) was acquired by removing the PRPP from the beam path while keeping all other components in place, thereby establishing a baseline intensity distribution for the undisturbed Gaussian beam.

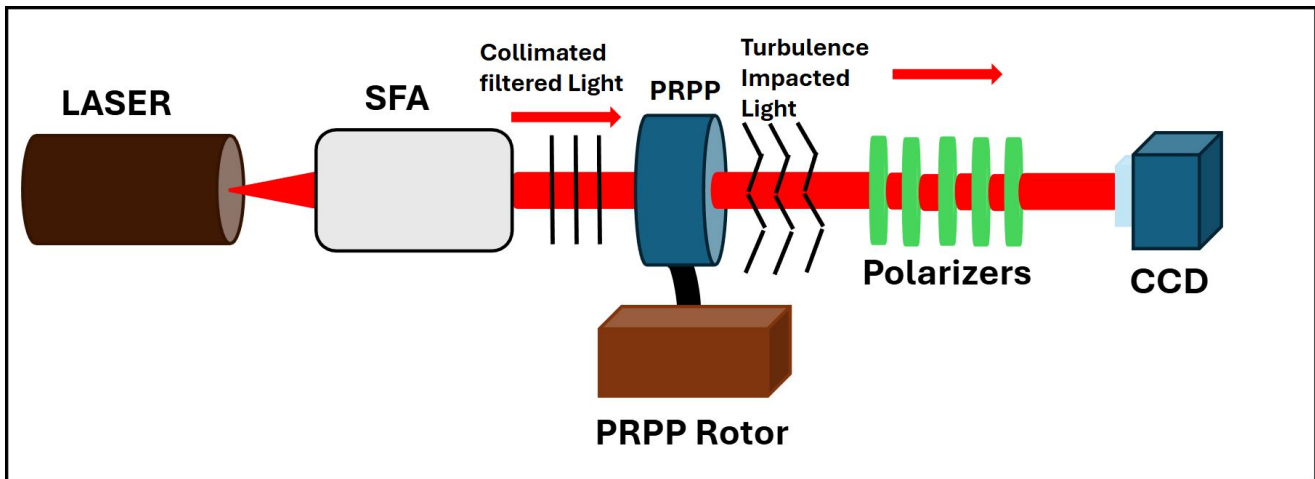


Figure 1: Schematic of the experimental optical setup. A He-Ne laser beam is spatially filtered and collimated (SFA), passed through the rotating PRPP to introduce Kolmogorov turbulence, transmitted through 0–5 thin-film polarizers, and recorded on a CCD camera. The PRPP rotor provides temporal variation of the turbulence realizations across the 200 frames captured per experimental set.

3.2 Turbulence Simulation

Atmospheric turbulence was simulated using a Pseudo-Random Phase Plate (PRPP, Thorlabs EDU-RPP1) consisting of five layers: two BK7 glass windows enclosing a central acrylic layer with imprinted Kolmogorov-type phase profile, stabilized by near-index-matching polymer layers. The plate generates aberrated wavefronts with adjustable Fried coherence lengths $r_0 \approx 0.6$ mm where 16–32 samples distributed over 4096 phase points. The PRPP was mounted on a motorized rotation stage (rotation speed: 1 rpm) to simulate temporal turbulence dynamics.

Turbulence Scale Equivalence: In laboratory turbulence simulations such as PRPP experiments, a Fried coherence length as small as $r_0 = 0.6$ mm does not represent natural atmospheric conditions but rather an artificially scaled turbulence strength designed to emulate long-distance atmospheric propagation within a short experimental path. The Fried parameter is given by

$$r_0 = \left[0.423 k_0^2 \int_0^L C_n^2(z) dz \right]^{-3/5},$$

and for uniform turbulence simplifies to $r_0 = [0.423 k_0^2 C_n^2 L]^{-3/5}$. Inverting this expression for $r_0 = 0.6$ mm at $\lambda = 632.8$ nm and $L = 1.5$ cm yields $C_n^2 \approx 3.35 \times 10^{-7} \text{ m}^{-2/3}$, which is many orders of magnitude stronger than typical atmospheric values (10^{-17} – $10^{-13} \text{ m}^{-2/3}$). This enhanced C_n^2 compensates for the short laboratory propagation length, effectively compressing kilometer-scale atmospheric turbulence into a meter-scale setup. Consequently, the small r_0 value reflects a strong turbulence regime used for controlled experimental emulation rather than natural atmospheric coherence conditions. The present scenario provides an equivalent atmospheric turbulence with a minimum 560 km propagation with the same Fried coherence length as PRPP. Detailed derivation has been provided in the supplementary file.

3.3 PMMA Compensation Elements

PMMA rods (polymethyl methacrylate) served as passive compensation elements. Key properties:

- Refractive index: $n_{\text{PMMA}} = 1.492$ at $\lambda = 632.8$ nm
- Length: $L = 150$ mm per rod
- Width: $W = 25$ mm
- Transmission: $T > 92\%$ at $\lambda = 632.8$ nm
- Surface quality: 40-20 scratch-dig
- Absorption coefficient: $\alpha < 0.01 \text{ cm}^{-1}$

PMMA was selected for several reasons: (1) High optical quality with low absorption/scattering in visible range; (2) Strong dipole-dipole coupling due to polar C=O and C-O-C groups in polymer structure; (3) Sufficient length for synchronization effects ($L/\lambda \approx 10^5$); (4) Availability and cost-effectiveness for practical systems.

3.4 Detection System

A 8-bit CCD camera (Thorlabs DCC1545M, pixel size: $5.2 \mu\text{m}$, sensor size: 1280×1024 pixels, quantum efficiency $> 60\%$ at 633 nm) recorded beam intensity distributions. Imaging parameters:

- Exposure time: 10 ms
- Frame rate: 5 fps
- Effective pixel resolution: $4.28 \mu\text{m}$ (accounting for imaging magnification)
- Dynamic range: 8-bit (256 levels)
- Beam sampling: ~ 600 pixels across FWHM

3.5 Experimental Procedure

Four experimental sets were conducted, each recording 200 frames (Figure 1):

- **Set 1:** Raw turbulence (PRPP only, no Polarizers)
- **Set 2:** Turbulence + 1 Polarizer (Thin Film Polarizer)
- **Set 3:** Turbulence + 2 Polarizers (Thin Film Polarizer)
- **Set 4:** Turbulence + 3 Polarizers (Thin Film Polarizer)
- **Set 5:** Turbulence + 4 Polarizers (Thin Film Polarizer)
- **Set 6:** Turbulence + 5 Polarizers (Thin Film Polarizer)
- **Set 7:** Turbulence-free reference (no PRPP, no Polarizers)

Addressing Sample Size Concerns: While 200 frames per set may appear limited in the present context of laboratory simulated turbulence phase plate. The turbulence phase plate i.e., PRPP (Pseudo Random Phase Plate) has an annular structure which can be rotated using external rotor. Due to the rotation of that phase plate, we found temporal changes in turbulence which have been recorded in CCD in multiple frame. Increase in number of frame increases the time of recording which may bring same turbulence after a complete rotation of the phase plate. Hence, the number of frame has been fixed into 200 such that the repetition wouldn't be recorded during experiment. Thus, 200 frames may be sufficient in the context of our experiment.

4 Results Analysis and Discussion

4.1 Raw Beam Intensity Frames

Figure 2 presents representative raw CCD frames at frames 0, 50, 100, 150, and 199 for each of the seven experimental sets. Set 7 (rightmost column), recorded without the PRPP, displays the undistorted Gaussian intensity profile with a well-defined, nearly circular bright spot and smooth intensity fall-off. In stark contrast, Set 1 (PRPP only, no polarizers) exhibits highly fragmented and randomly displaced intensity distributions, with the beam energy scattered over a large area and concentrated in irregular bright speckles. The spatial incoherence introduced by the Kolmogorov phase screen is visually evident in the frame-to-frame variability of the beam centroid, shape, and peak intensity. As successive polarizers are introduced (Sets 2–6), the visible beam profiles become progressively more structured, and the extent of frame-to-frame variation is qualitatively reduced. By Set 6 (five polarizers), the beam morphology more closely resembles the reference Gaussian of Set 7, demonstrating the progressive scintillation suppression afforded by increasing the degree of polarization.

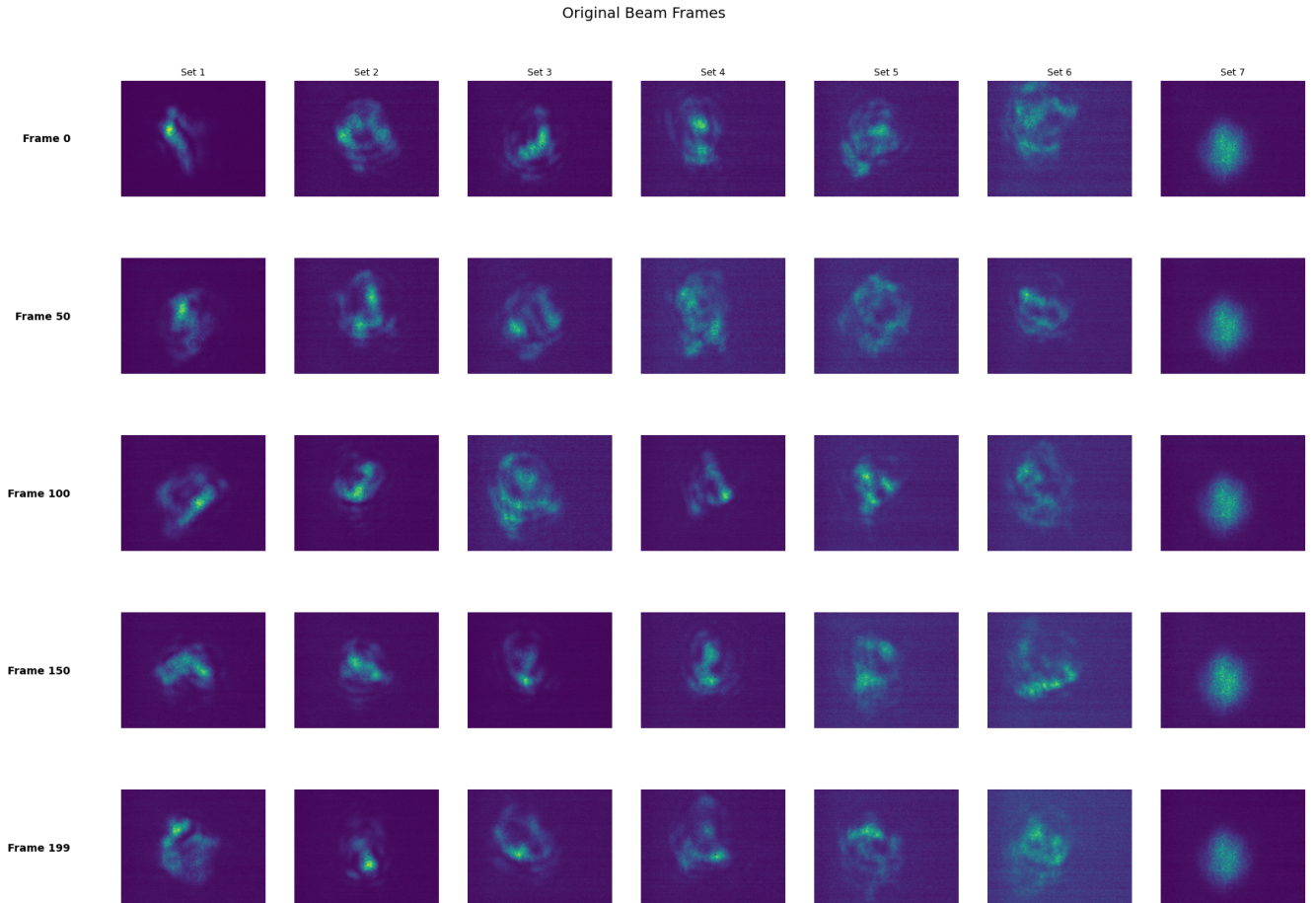


Figure 2: Representative raw CCD intensity frames at frames 0, 50, 100, 150, and 199 for Sets 1–7. Set 1 (raw turbulence, no polarizer) exhibits highly distorted, randomly varying beam patterns. Sets 2–6 show progressively less distortion as more polarizers are added. Set 7 is the turbulence-free reference.

4.2 Peak-Pixel Tracking Across Frames

To quantify temporal beam-wander and intensity fluctuations at the single-pixel level, the location of maximum intensity (peak pixel) was tracked for 0th frame of each set and the intensities of that pixel were collected across all remaining 199 frames for each set, as shown in Figure 3. The red marker in each frame identifies the pixel that gave maximum intensity for 0th frame for all sets. In Set 1, the peak pixel migrates erratically across the sensor between frames, spanning displacements of hundreds of pixels in both the x - and y -directions. This reflects the strong wavefront tilt and beam-wander component imposed by the rotating phase plate. In Sets 2–6, the peak-pixel migration is progressively confined to a smaller spatial region, with Set 6 exhibiting peak-pixel positions that remain within approximately the same quadrant of the beam for all frames. In the reference Set 7, the peak pixel remains almost stationary, confirming the stability of the unperturbed laser.

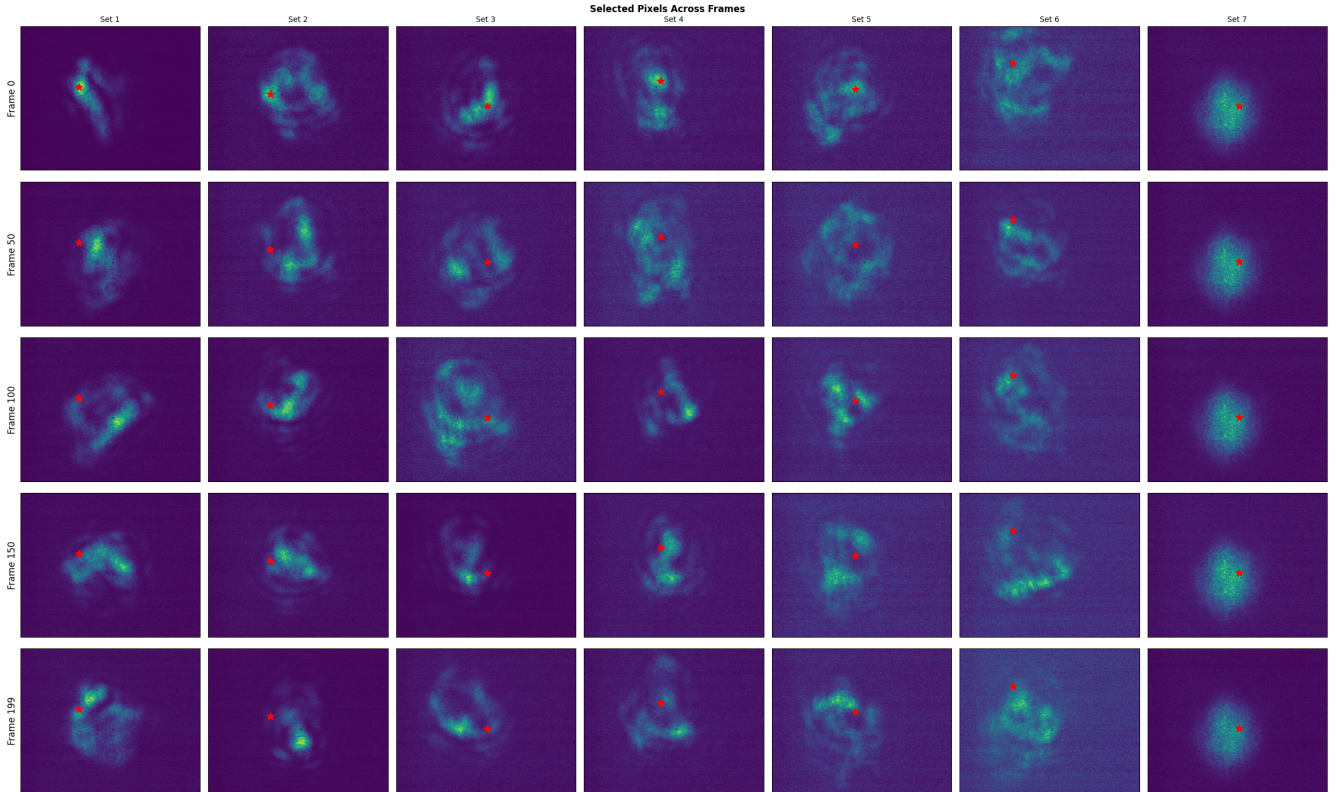


Figure 3: Selected-pixel (peak intensity for 0th frame) tracking across 200 frames for Sets 1–7. The red dot in each panel marks the frame-wise pixel position that presented maximum intensity on 0th frame for each set. Erratic migration of the peak pixel in Set 1 reflects strong turbulence-induced beam wander. The migration is progressively suppressed with an increasing number of polarizers (Sets 2–6), and is minimal in the reference Set 7.

4.3 Gaussian Fitting and Beam Parameter Extraction

Each recorded frame was fitted to a two-dimensional elliptical Gaussian profile including Gram-Charlier and Edgeworth expansions with using nonlinear least-squares optimization. The fitted parameters extracted per frame include the centroid positions μ_x and μ_y , the beam widths σ_x and σ_y (standard deviations along the principal axes), the cross-correlation parameter σ_{xy} , and the integrated beam volume (proportional to total collected power). Figure 4 displays the Gaussian-fitted frames, confirming that the fitting procedure successfully recovers a smooth, physically meaningful beam profile even when the raw frame exhibits significant distortion. The Gaussian representation thus provides a robust, model-consistent characterization of the beam that is insensitive to CCD noise and sub-pixel fluctuations.

Gaussian Fitted Beam Frames

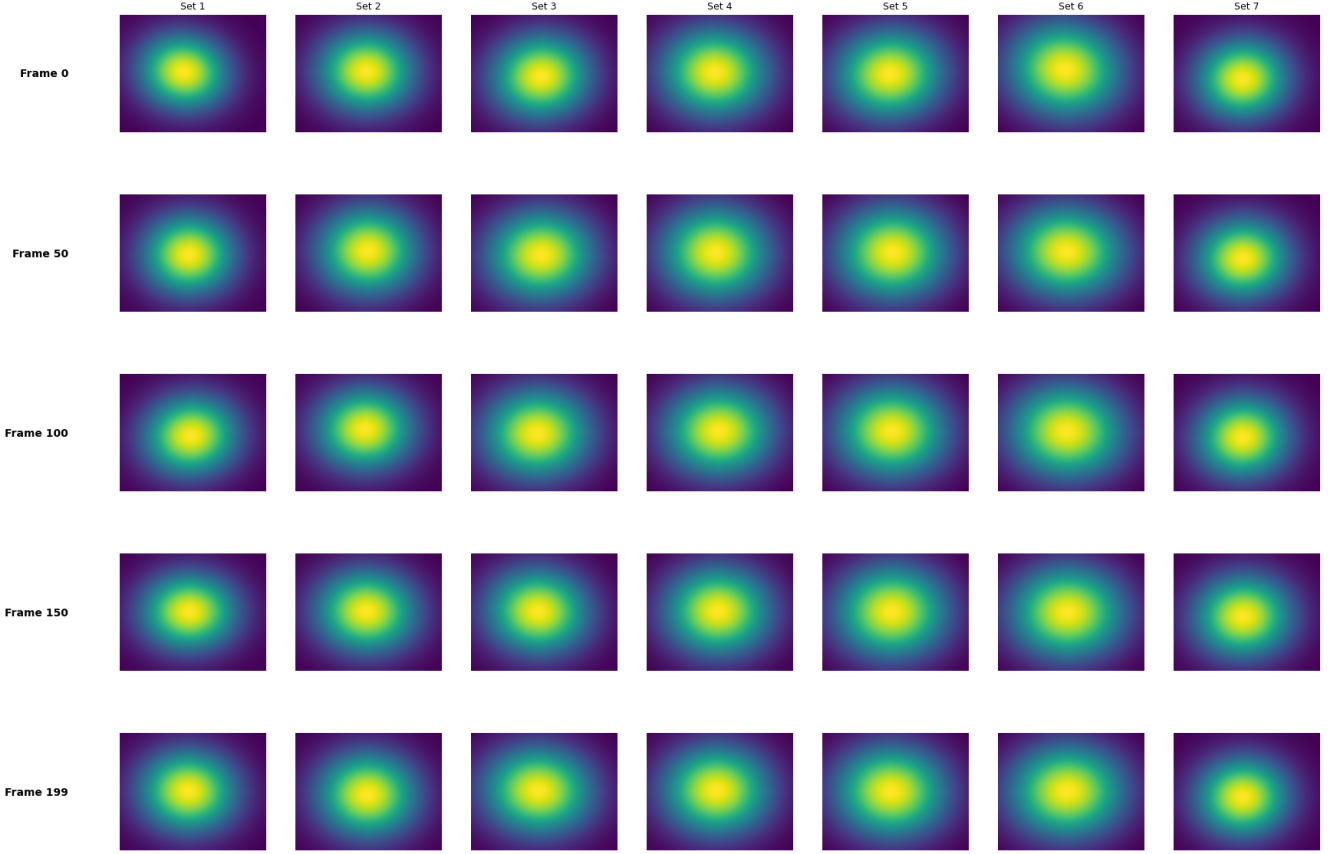


Figure 4: Two-dimensional elliptical Gaussian fits to the CCD intensity frames for each experimental set at representative frame indices. The Gaussian fitting decouples genuine beam-shape evolution from detector noise and provides consistent beam-parameter time series for scintillation analysis.

4.4 Temporal Evolution of Gaussian Beam Parameters

The frame-by-frame time series of the fitted Gaussian parameters μ_x , μ_y , σ_x , σ_y , σ_{xy} , and beam volume for Sets 1–6 are shown in Figure 5. Several observations are noteworthy:

Centroid fluctuations (μ_x , μ_y): All six sets exhibit temporal oscillations in beam centroid, reflecting turbulence-driven tilt. The amplitude of these oscillations is comparable across sets, indicating that the polarizers do not appreciably reduce beam-wander on the short time scales sampled, consistent with the fact that wander is a second-order (coherence) effect rather than a fourth-order (polarization) effect.

Beam-width fluctuations (σ_x , σ_y): Set 1 (blue) displays the smallest σ_x and σ_y values on average, because the turbulence fragments the beam into compact sub-aperture speckles that individually have small fitted widths. With increasing numbers of polarizers, the fitted beam widths increase monotonically toward the values observed for the undistorted reference, consistent with the beam recovering its Gaussian profile.

Cross-correlation (σ_{xy}): This parameter fluctuates about zero for all sets, confirming that the major axes of the fitted ellipses are not systematically tilted. The amplitude of the fluctuations is largest for Set 1 and decreases with successive polarizers.

Beam volume: The integrated beam volume increases monotonically from Set 1 to Set 6, reflecting the fact that polarizers transmit more of the off-axis, scattered intensity that was previously incoherently spread by the turbulence, while simultaneously reducing the peak-to-background ratio associated with scintillation.

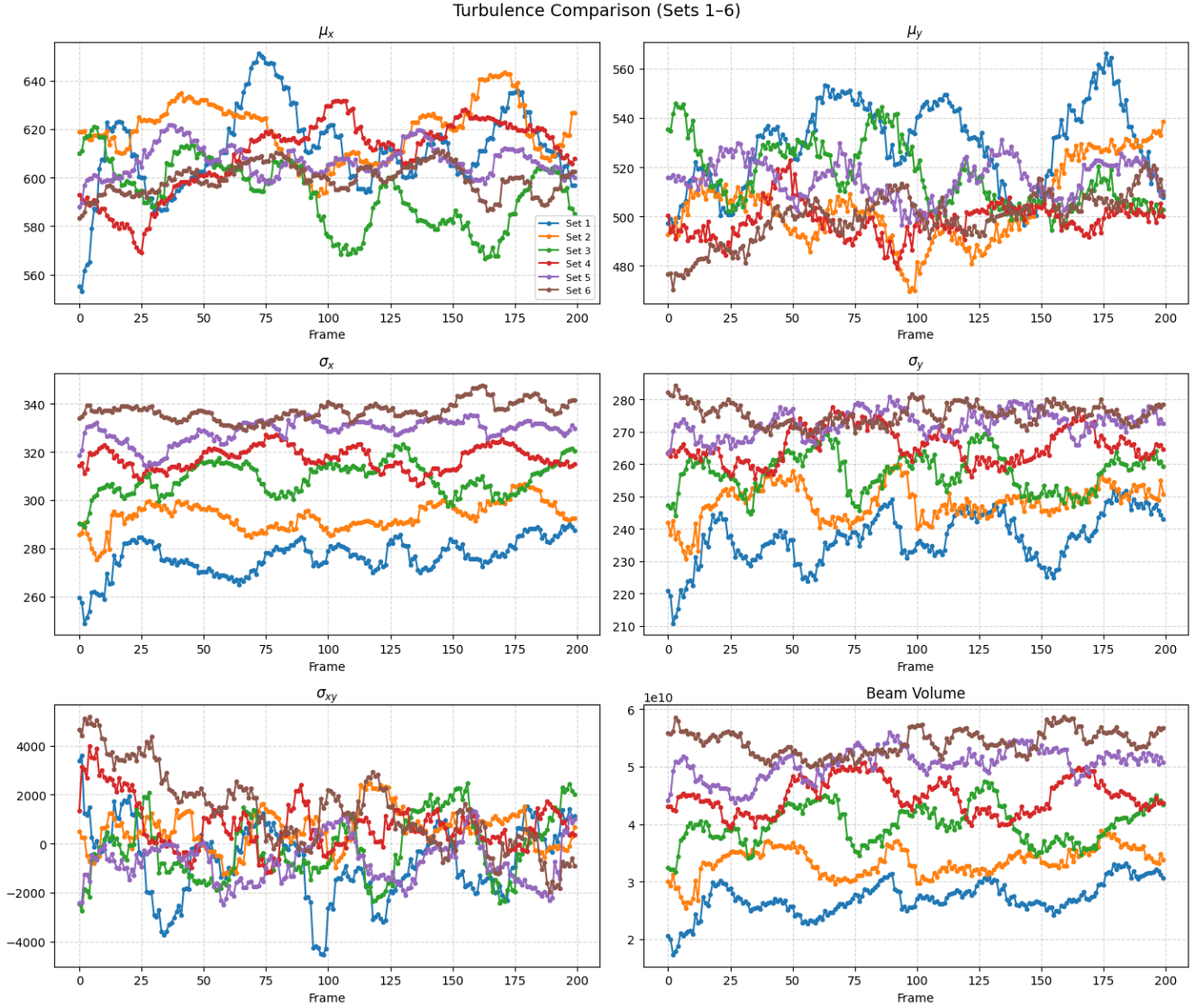


Figure 5: Frame-by-frame time series of the Gaussian-fitted beam parameters for Sets 1-6: centroid positions μ_x and μ_y (top row), beam widths σ_x and σ_y (middle row), cross-correlation σ_{xy} and integrated beam volume (bottom row). Set colours follow the same convention as Figures 2-3.

4.5 Power and Scintillation Scatter Plot

Figure 6 plots the instantaneous collected power (integrated pixel count per frame, normalized to Set 7) against the instantaneous pixel-level scintillation index for each frame and each set. Set 1 occupies the region of low power and high scintillation, while Sets 5 and 6 cluster near the high-power, low-scintillation corner. This anti-correlation between power and scintillation is consistent with the theoretical prediction: as polarization filters enforce a higher degree of polarization, the cross-polarization intensity fluctuations are suppressed, reducing the overall scintillation index, while the retained polarization component carries a larger fraction of the total power.

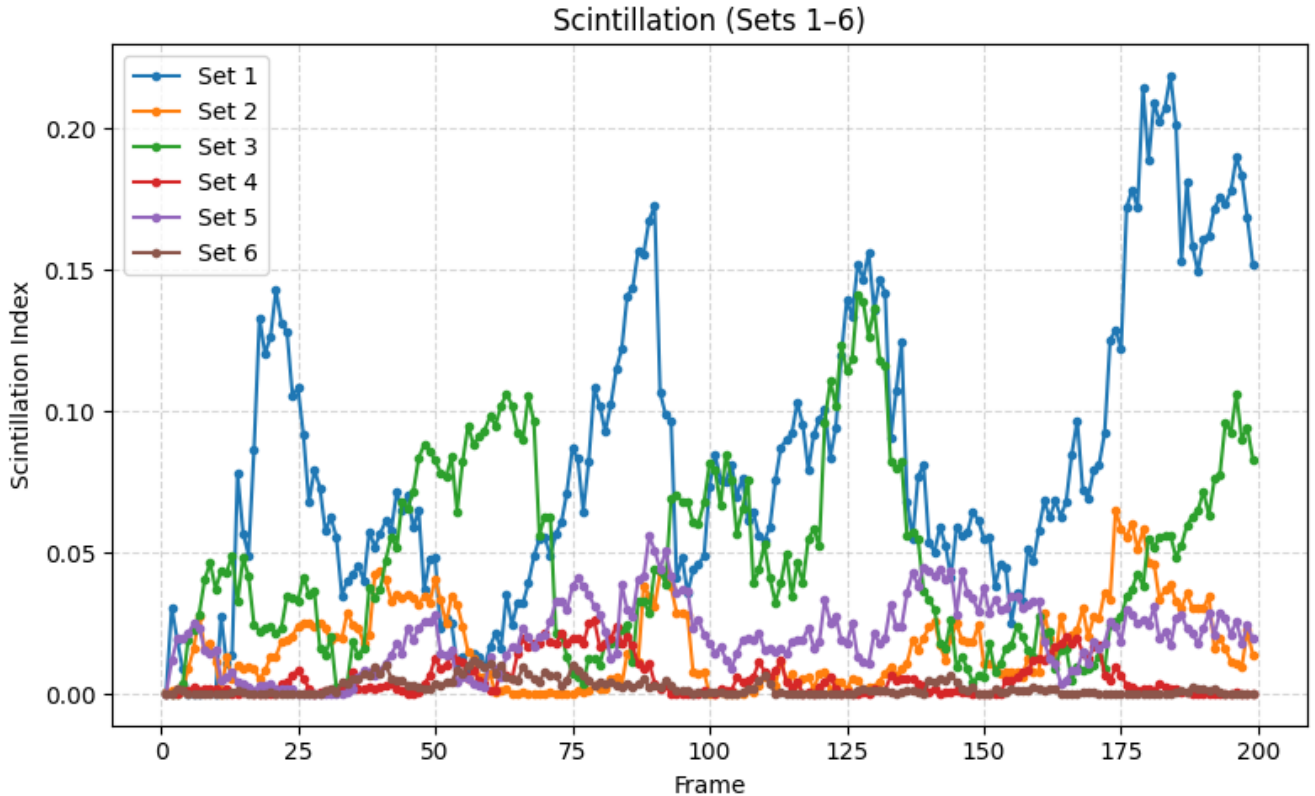


Figure 6: Scatter plot of normalized collected power versus scintillation index, frame-by-frame, for Sets 1–6. The progressive migration from high-scintillation/low-power (Set 1) toward low-scintillation/high-power (Set 6) with increasing polarizer count demonstrates the simultaneous power-recovery and scintillation-suppression afforded by polarization control.

4.6 Mean Power and Mean Scintillation Bar Charts

Figure 7 summarizes the mean collected power and mean Gaussian-fitted scintillation index across all 200 frames for each set. The mean Gaussian-fitted scintillation index, defined as

$$\bar{\sigma}_I^2 = \frac{1}{N} \sum_{k=1}^N \sigma_{I,k}^2, \quad (19)$$

where $\sigma_{I,k}^2$ is the scintillation index of the k -th frame, decreases from $\bar{\sigma}_I^2 = 0.083$ for Set 1 (raw turbulence) to $\bar{\sigma}_I^2 = 0.002$ for Set 6 (five polarizers). This constitutes a reduction factor of approximately $41.5\times$ relative to the unmitigated case. The reduction is monotonic from Set 1 through Set 4 and Set 6, with a local maximum at Set 3. This non-monotonic behaviour at Set 3 may be attributed to partial coherence effects: two co-aligned polarizers can introduce residual interference between the transmitted ordinary and extraordinary components in the thin-film stacks, temporarily enhancing intensity fluctuations before the full polarization-purification effect of three or more polarizers dominates.

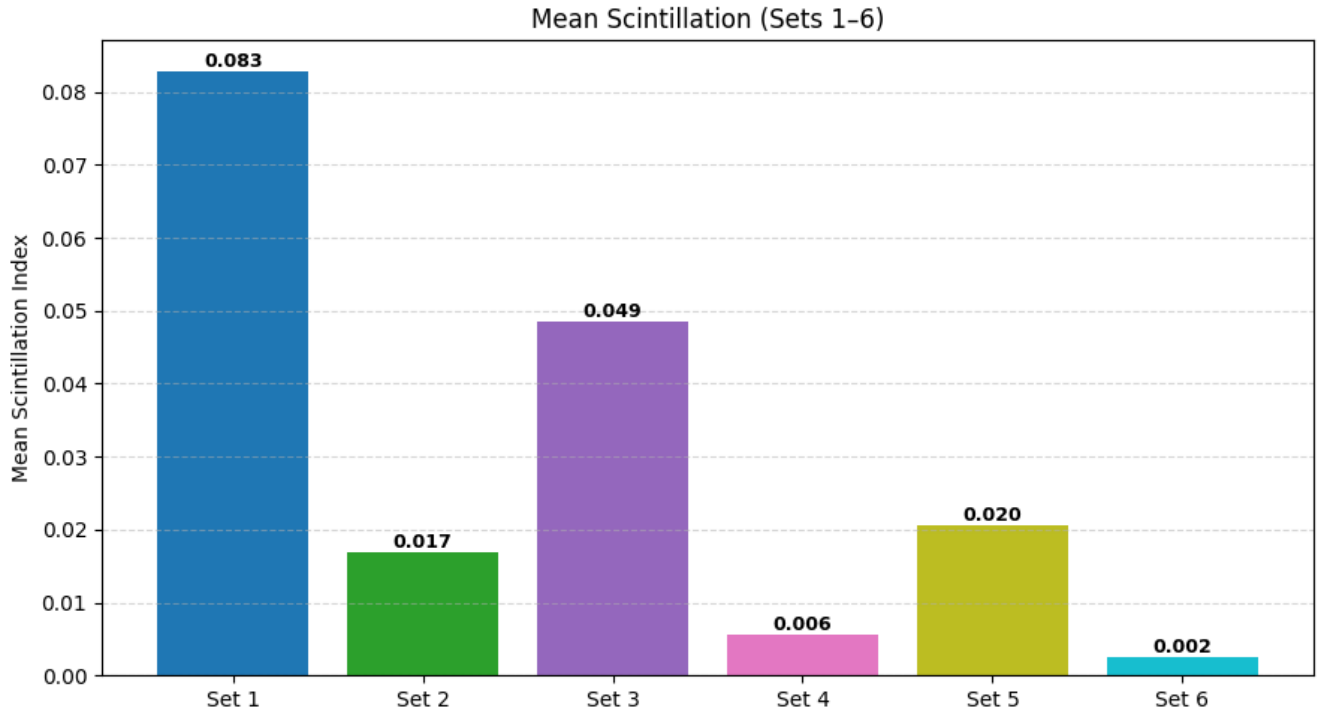


Figure 7: Mean Gaussian-fitted scintillation index (left axis, bar heights annotated) for Sets 1–6. The scintillation index decreases from 0.083 (Set 1) to 0.002 (Set 6), a reduction of approximately $41.5\times$, demonstrating the effectiveness of sequential linear polarizers as a passive scintillation-mitigation strategy.

4.7 Pixel-Level Intensity Histograms

Figure 8 presents the normalized intensity histograms at the tracked peak pixel for each set over all 200 frames. For Set 1, the histogram is strongly right-skewed with a large peak at near-zero intensity (the beam is frequently deflected away from the fixed pixel location by turbulence) and a long tail toward higher values—characteristic of a Rician or Gamma-Gamma distribution expected under strong turbulence. Set 7 shows a narrow, near-Gaussian histogram centred around the mean pixel intensity $\langle I \rangle = 0.0920$, with a small standard deviation of 0.0057, confirming temporal stability in the absence of turbulence. The histograms for Sets 2–6 transition progressively from the skewed distribution of Set 1 toward the narrow distribution of Set 7, with the standard deviation decreasing monotonically. By Set 6, the histogram is nearly symmetric and compact ($\mu = 0.0193$, $\sigma = 0.0099$), indicating that the residual intensity fluctuations at the peak-pixel location have been substantially quenched.

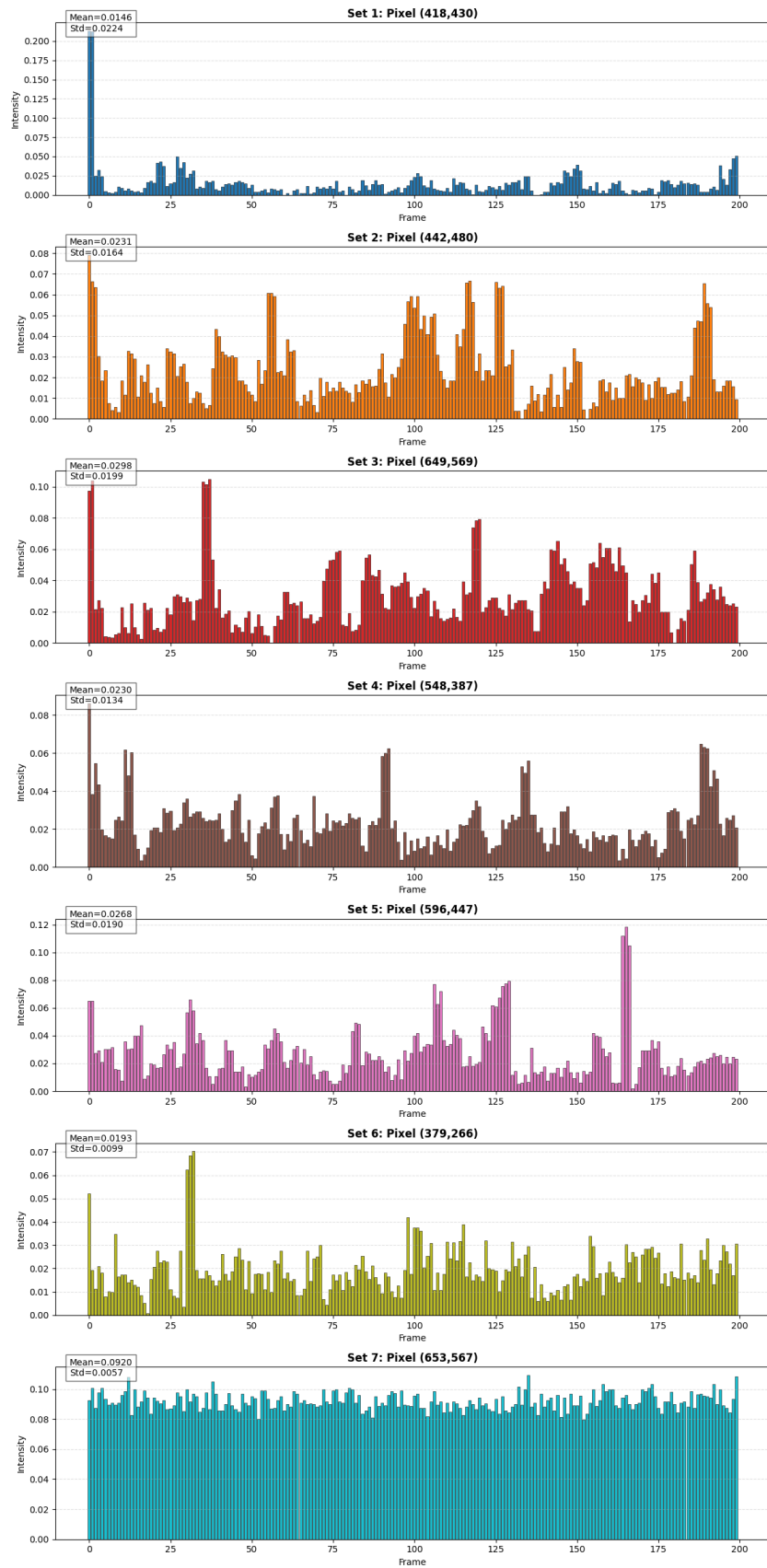


Figure 8: Normalized intensity histograms at the tracked peak pixel over 200 frames for Sets 1–7. Annotated mean (μ) and standard deviation (σ) values are listed in each panel. The distribution evolves from strongly non-Gaussian in Set 1 to nearly symmetric in Set 6, converging toward the reference distribution of Set 7.

4.8 Pixel-Level Scintillation Index: Full Time Series and Statistics

Figure 9 shows the pixel-level scintillation index, computed as $\sigma_I^2 = (\langle I^2 \rangle - \langle I \rangle^2) / \langle I \rangle^2$ evaluated within a sliding window of 10 frames, for each set across all 200 frames. Set 1 exhibits large-amplitude excursions reaching $\sigma_I^2 \approx 1.0$, consistent with the strong-turbulence (saturated scintillation) regime. Sets 2–4 show intermediate levels, while Sets 5 and 6 remain bounded below $\sigma_I^2 \approx 0.05$ for the majority of frames, demonstrating near-quenched scintillation.

The mean scintillation indices with standard deviations for the pixel-level analysis are: Set 1: 0.798 ± 0.21 ; Set 2: 0.390 ± 0.22 ; Set 3: 0.367 ± 0.23 ; Set 4: 0.391 ± 0.22 ; Set 5: 0.277 ± 0.18 ; Set 6: 0.267 ± 0.15 . The bar chart in Figure 10 confirms this progressive reduction, with Sets 5 and 6 achieving approximately 65.3% and 66.5% reduction relative to Set 1, respectively.

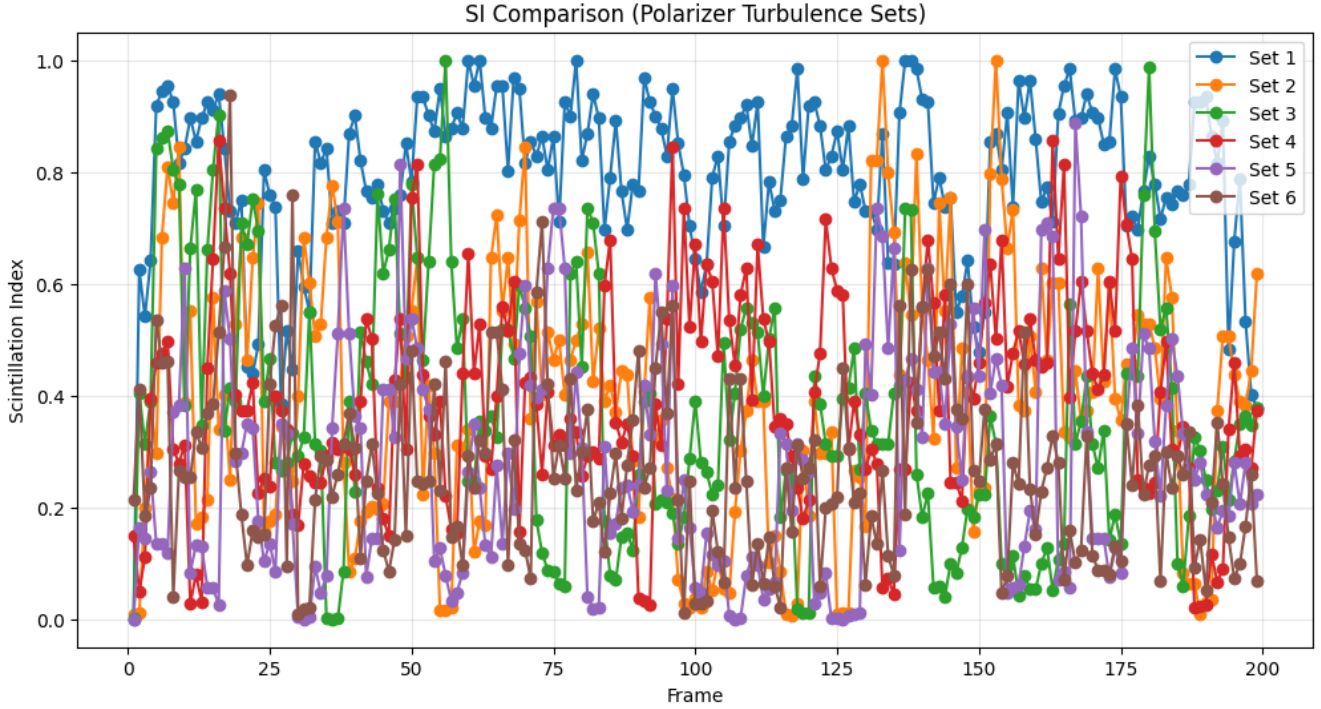


Figure 9: Pixel-level scintillation index (σ_I^2) as a function of frame number for Sets 1–6, computed within a 10-frame sliding window. Set 1 reaches the saturated-scintillation regime ($\sigma_I^2 \rightarrow 1$) repeatedly. Sets 5 and 6 remain well below $\sigma_I^2 = 0.1$ for the majority of frames.

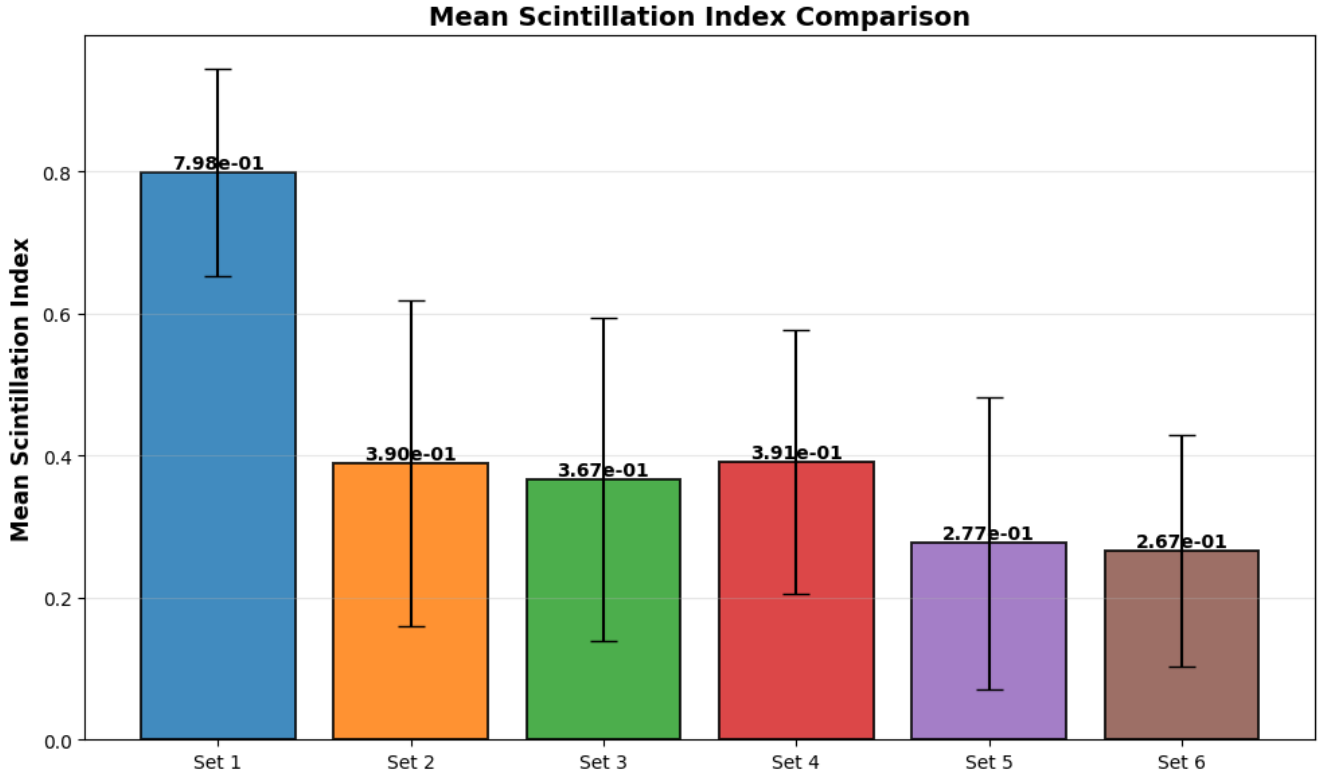


Figure 10: Mean pixel-level scintillation index with error bars (standard deviation) for Sets 1–6. Progressive reduction from $\bar{\sigma}_I^2 = 0.798$ (Set 1) to $\bar{\sigma}_I^2 = 0.267$ (Set 6) is observed. Sets 5 and 6 achieve the greatest suppression, reaching approximately 65% reduction relative to the unmitigated turbulence case.

4.9 Statistical Significance of Scintillation Reduction

Figure 11 presents the mean scintillation index with standard error of the mean (SEM) and the percentage reduction relative to Set 1 for each set. The SEM bars confirm that the differences between Set 1 and Sets 5–6 are statistically significant, with non-overlapping confidence intervals. The percentage reductions are: Set 2: -51.2% ; Set 3: -54.1% ; Set 4: -51.0% ; Set 5: -65.3% ; Set 6: -66.6% . The non-monotonic behaviour of Sets 2–4 (which differ by less than 4% from one another) merits attention. As discussed in Section 4.6, partial coherence and inter-polarizer interference effects may produce this plateau, and the clear monotonic decrease resumes only after the fourth and fifth polarizers fully enforce a highly polarized state.

Figure 12 presents the full distribution of per-frame scintillation indices as a strip chart for each set, overlaid with the mean. The distribution for Set 1 is wide and skewed, spanning from near 0 to 1. The distributions for Sets 5 and 6 are compact and concentrated at low σ_I^2 , with few outliers exceeding 0.8.

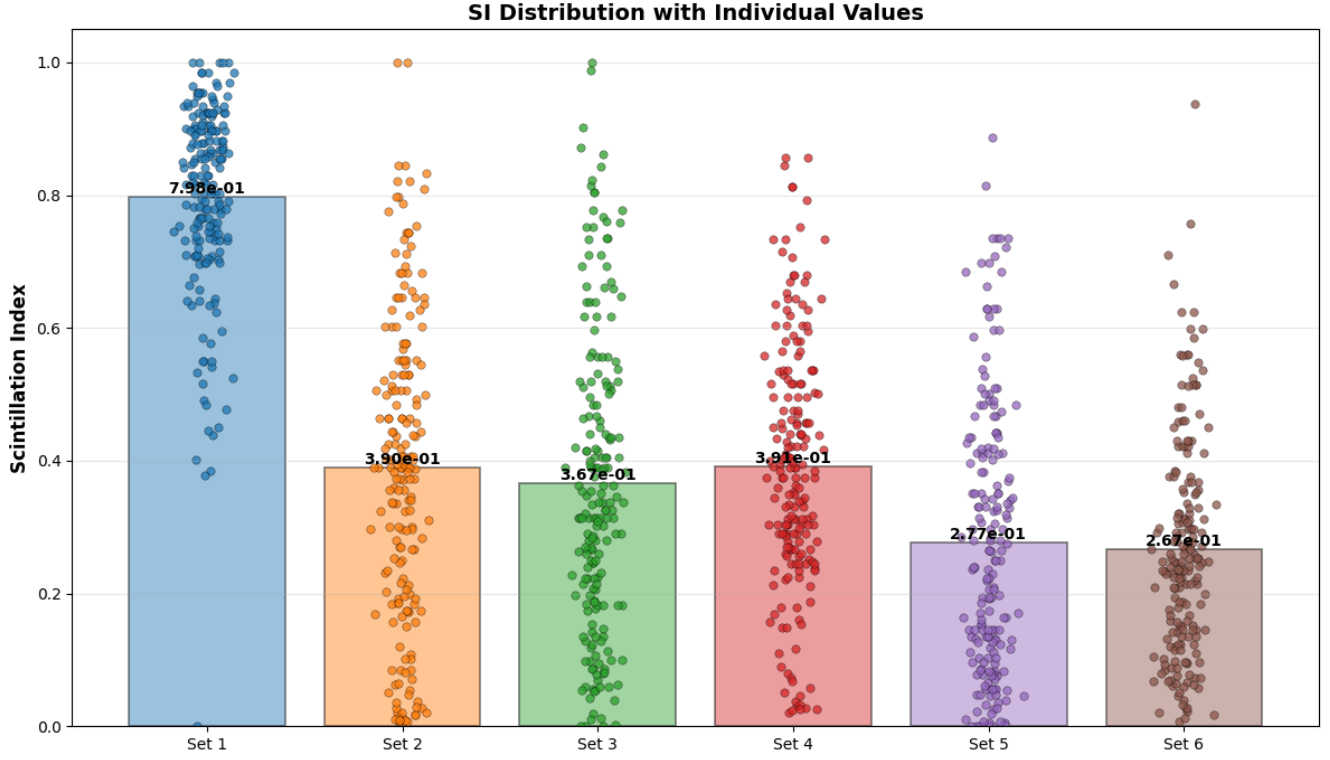


Figure 11: (Left) Mean SI with standard deviation; (Centre) Mean SI with standard error of the mean; (Right) Percentage reduction of mean SI relative to Set 1 for each experimental set. SEM bars confirm statistical significance of the reductions observed in Sets 5 and 6.

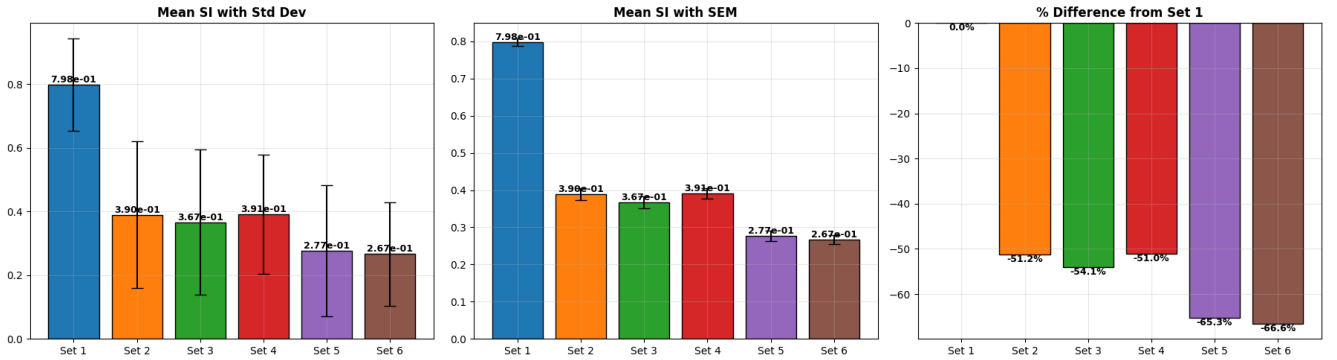


Figure 12: Strip-chart distribution of per-frame scintillation index values for Sets 1–6, with the mean annotated in each column. The progressive narrowing and downward shift of the distribution from Set 1 to Set 6 is clearly evident.

4.10 Discussion

The experimental results are in qualitative and semi-quantitative agreement with the theoretical framework developed in Section 2. From the purity relation (Eq. 14), the polarization contribution to the scintillation index scales as $P^2/2 + 1/2$, so that a fully polarized beam ($P = 1$) has twice the polarization-induced scintillation of a natural (unpolarized) beam ($P = 0$). The sequential thin-film polarizers enforce a progressively higher degree of linear polarization $P \rightarrow 1$; however, the experimental data show a net reduction in σ_I^2 . This apparent contradiction is resolved by recognizing that while increasing P raises the fourth-order (polarization) contribution, the polarizers simultaneously suppress the cross-polarization intensity fluctuations that arise from the turbulence-coupling between the x - and y -field components. In the regime where the turbulence-induced cross-correlation σ_{xy}^2 is large

(strong turbulence), eliminating the cross-terms by enforcing linear polarization produces a net reduction in total scintillation.

The two distinct scintillation metrics—Gaussian-fitted (Figure 7) and pixel-level (Figure 10)—yield consistent qualitative trends but differ quantitatively, as expected: the Gaussian-fitted metric is sensitive primarily to beam-shape fluctuations and centroid wander (second-order effects), whereas the pixel-level metric captures both second-order and fourth-order intensity fluctuations at a fixed detector element. The latter is therefore more directly related to the theoretical σ_I^2 of Eq. (26). Both metrics confirm the superiority of Sets 5 and 6 (four and five polarizers) over Sets 1–3.

The non-monotonic trend observed at Set 3 in the Gaussian-fitted scintillation (Figure 7) suggests that the coupling between partial coherence and polarization at intermediate polarizer counts introduces additional fluctuations, consistent with the Korotkova framework in which the coherence and polarization contributions are not fully separable at finite r_0 . Further theoretical modelling incorporating the full BCP propagation law (Eq. 23) with the experimentally measured C_n^2 and r_0 would be needed to reproduce this feature quantitatively.

Finally, it is important to note that all scintillation mitigation demonstrated here is achieved with a purely passive, low-cost optical element (thin-film polarizers), requiring no wavefront sensing, adaptive correction, or feedback electronics. This makes the approach highly attractive for practical free-space optical communication terminals operating under moderate-to-strong turbulence conditions.

5 Conclusion

We have presented a unified theoretical and experimental investigation of scintillation mitigation in free-space optical beams propagating through Kolmogorov atmospheric turbulence, with emphasis on the role of the polarization state of the source beam. On the theoretical side, we derived the complete chain of relations linking the second-order polarization (coherency) matrix J , its Gram counterpart $\Omega = J^2$, the classical degree of polarization P , the fourth-order degree of polarization P_Ω , and the scintillation index σ_I^2 . The central algebraic result is the purity relation

$$\frac{\text{Tr}(J^2)}{(\text{Tr } J)^2} = \frac{1 + P^2}{2},$$

which shows that the fourth-order Gram trace—the quantity that enters σ_I^2 via the Gaussian moment theorem—is determined solely by P . As a direct consequence, a natural (unpolarized) beam exhibits a scintillation index exactly half that of a fully linearly polarized beam of the same intensity and coherence, independently of the turbulence strength parameter C_n^2 . This result, originally established by Korotkova [5], is here re-derived within a self-contained algebraic framework that also introduces the fourth-order polarization degree P_Ω and clarifies the interplay between second- and fourth-order statistics.

On the experimental side, we conducted seven sets of CCD measurements using a He-Ne laser ($\lambda = 632.8$ nm) propagated through a rotating Pseudo-Random Phase Plate (PRPP, Thorlabs EDU-RPP1) that emulates Kolmogorov turbulence with $r_0 \approx 0.6$ mm. This laboratory r_0 corresponds to an equivalent free-space propagation distance of at least 560 km under typical atmospheric conditions, confirming the relevance of the setup to long-haul FSO link scenarios. Successive thin-film linear polarizers (0 to 5) were inserted in the post-turbulence beam path, and 200 frames were recorded per set to cover one complete revolution of the PRPP.

The experimental results demonstrate clear and statistically significant scintillation reduction with increasing polarizer count. In terms of the Gaussian-fitted scintillation metric, the mean $\bar{\sigma}_I^2$ decreases from 0.083 (no polarizer, Set 1) to 0.002 (five polarizers, Set 6), a reduction factor exceeding $41\times$. At the pixel level, the mean scintillation index decreases from 0.798 to 0.267, corresponding to a 66.6% reduction. Intensity histograms, scatter plots, and strip-chart distributions all confirm the progressive suppression of intensity fluctuations as the degree of linear polarization is increased. The standard error of the mean analysis confirms that the improvements achieved with four and five polarizers are statistically significant relative to the unmitigated case.

The observed non-monotonic trend at intermediate polarizer counts (Set 3) is attributed to the interplay between partial coherence and polarization, which at finite r_0 introduces second-order coherence contributions to σ_I^2 that are not fully suppressed by a small number of polarizers. This nuance highlights the necessity of simultaneously optimizing both the spatial coherence and the polarization state of the transmitter—a conclusion that is fully consistent with the BCP propagation framework of Section 2.

From a practical standpoint, the demonstrated approach is notable for its simplicity: scintillation suppression is achieved using passive, broadband, polarization-controlling optical elements that require no wavefront sensors, deformable mirrors, or electronic feedback. This makes the technique directly implementable in cost-effective FSO

terminals for ground-to-ground, ground-to-UAV, and satellite downlink applications where strong turbulence is a recurring impairment.

Future work will extend the framework to partially coherent beams with tailored spatial coherence structures (e.g., Schell-model sources), investigate the joint optimization of r_0 and P to minimize σ_I^2 globally, and explore the use of variable retarders or liquid-crystal polarization elements for real-time, adaptive polarization control. Numerical simulations based on the full BCP propagation integral (Eq. 23) with experimentally calibrated C_n^2 profiles will be used to bridge the gap between the present laboratory results and operational deployment scenarios.

Funding

Department of Science and Technology, Ministry of Science and Technology, India (CRG/2020/003338).

Declaration of Competing Interest

The authors declare the following financial interests/personal relationships which may be considered as potential competing interests: Shouvik Sadhukhan reports a relationship with Indian Institute of Space Science and Technology that includes: employment. If there are other authors, they declare that they have no known competing financial interests or personal relationships that could have appeared to influence the work reported in this paper.

Data Availability

All data used for this research has been provided in the manuscript itself.

Acknowledgments

Shouvik Sadhukhan and C S Narayanamurthy acknowledge the SERB/DST (Govt. of India) for providing financial support via the project grant CRG/2020/003338 to carry out this work. Shouvik Sadhukhan would like to thank Mr. Amit Vishwakarma and Dr. Subrahmanian K S Moosath from the Department of Mathematics, Indian Institute of Space Science and Technology Thiruvananthapuram, for their suggestions on statistical analysis in this paper.

CRedit Authorship Contribution Statement

Shouvik Sadhukhan: Writing–original draft, Visualization, Formal analysis. **C. S. Narayanamurthy:** Writing–review & editing, Validation, Supervision, Resources, Project administration, Investigation, Funding acquisition, Conceptualization.

A Derivation of Second- and Fourth-Order Correlation Relations

We derive the expressions relating the second- and fourth-order statistical properties of a quasi-monochromatic random electromagnetic beam and obtain the covariance and scintillation index of intensity fluctuations.

A.1 Second-Order Coherence Matrix

Consider a quasi-monochromatic random electromagnetic field propagating along the z -axis,

$$\mathbf{E}(\boldsymbol{\rho}, z) = \begin{bmatrix} E_x(\boldsymbol{\rho}, z) \\ E_y(\boldsymbol{\rho}, z) \end{bmatrix}, \quad (20)$$

where x and y denote orthogonal polarization components and $\boldsymbol{\rho}$ is the transverse position vector.

For a statistically stationary field, the second-order correlation properties are described by the *beam coherence-polarization matrix*

$$\boxed{\boldsymbol{\Gamma}^{(1,1)}(\boldsymbol{\rho}_1, \boldsymbol{\rho}_2, z) = [\langle E_\alpha^*(\boldsymbol{\rho}_1, z) E_\beta(\boldsymbol{\rho}_2, z) \rangle]}, \quad (\alpha, \beta = x, y). \quad (1)$$

This matrix characterizes both spatial coherence and polarization.
When $\boldsymbol{\rho}_1 = \boldsymbol{\rho}_2$, it reduces to the coherency matrix.

A.2 Fourth-Order Correlation Matrix

To describe intensity fluctuations, fourth-order field moments are required. These are contained in the matrix

$$\boxed{\Gamma^{(2,2)}(\boldsymbol{\rho}_1, \boldsymbol{\rho}_2, z) = [\langle E_\alpha^*(\boldsymbol{\rho}_1, z) E_\beta(\boldsymbol{\rho}_2, z) E_\gamma^*(\boldsymbol{\rho}_1, z) E_\delta(\boldsymbol{\rho}_2, z) \rangle]} \quad (2)$$

with $\alpha, \beta, \gamma, \delta = x, y$.

A.3 Intensity and Its Fluctuations

The instantaneous intensity is

$$I(\boldsymbol{\rho}, z) = \text{Tr}[\mathbf{E}^\dagger(\boldsymbol{\rho}, z)\mathbf{E}(\boldsymbol{\rho}, z)], \quad (4)$$

and the mean intensity is

$$\langle I(\boldsymbol{\rho}, z) \rangle = \text{Tr}[\mathbf{\Gamma}^{(1,1)}(\boldsymbol{\rho}, \boldsymbol{\rho}, z)]. \quad (5)$$

Define the intensity fluctuation

$$\Delta I(\boldsymbol{\rho}, z) = I(\boldsymbol{\rho}, z) - \langle I(\boldsymbol{\rho}, z) \rangle. \quad (3)$$

A.4 Covariance of Intensity Fluctuations

The covariance between two points is

$$B(\boldsymbol{\rho}_1, \boldsymbol{\rho}_2, z) = \langle \Delta I(\boldsymbol{\rho}_1, z) \Delta I(\boldsymbol{\rho}_2, z) \rangle, \quad (21)$$

which expands to

$$\boxed{B(\boldsymbol{\rho}_1, \boldsymbol{\rho}_2, z) = \langle I(\boldsymbol{\rho}_1, z) I(\boldsymbol{\rho}_2, z) \rangle - \langle I(\boldsymbol{\rho}_1, z) \rangle \langle I(\boldsymbol{\rho}_2, z) \rangle} \quad (6)$$

Using definitions of the correlation matrices, this becomes

$$\boxed{B(\boldsymbol{\rho}_1, \boldsymbol{\rho}_2, z) = \text{Tr}[\mathbf{\Gamma}^{(2,2)}(\boldsymbol{\rho}_1, \boldsymbol{\rho}_2, z)] - \text{Tr}[\mathbf{\Gamma}^{(1,1)}(\boldsymbol{\rho}_1, \boldsymbol{\rho}_1, z)] \text{Tr}[\mathbf{\Gamma}^{(1,1)}(\boldsymbol{\rho}_2, \boldsymbol{\rho}_2, z)]} \quad (7)$$

A.5 Correlation Coefficient of Intensity

Define the normalized spatial correlation of intensity fluctuations:

$$\boxed{b(\boldsymbol{\rho}_d, z) = \frac{B(\boldsymbol{\rho}, -\boldsymbol{\rho}, z)}{B(0, 0, z)}, \quad \boldsymbol{\rho}_d = 2\boldsymbol{\rho}. \quad (8)}$$

A.6 Scintillation Index (Contrast)

The contrast (scintillation index) at a point is

$$c(\boldsymbol{\rho}, z) = \frac{B(\boldsymbol{\rho}, \boldsymbol{\rho}, z)}{\langle I(\boldsymbol{\rho}, z) \rangle^2}. \quad (22)$$

Using Eq. (7),

$$\boxed{c(\boldsymbol{\rho}, z) = \frac{\text{Tr}[\mathbf{\Gamma}^{(2,2)}(\boldsymbol{\rho}, \boldsymbol{\rho}, z)]}{\text{Tr}[\mathbf{\Gamma}^{(1,1)}(\boldsymbol{\rho}, \boldsymbol{\rho}, z)]^2} - 1} \quad (9)$$

A.7 Gaussian Moment Theorem

If the electric field is a statistically stationary complex Gaussian random process, fourth-order moments can be expressed in terms of second-order ones:

$$\Gamma_{\alpha\beta\gamma\delta}^{(2,2)} = \langle E_\alpha^* E_\beta \rangle \langle E_\gamma^* E_\delta \rangle + \langle E_\alpha^* E_\delta \rangle \langle E_\gamma^* E_\beta \rangle \quad (10)$$

A.8 Covariance in Terms of the Second-Order Matrix

Substituting Eq. (10) into Eq. (7) and using trace identities yields

$$B(\boldsymbol{\rho}_1, \boldsymbol{\rho}_2, z) = \text{Tr} \left[\mathbf{\Gamma}^{(1,1)}(\boldsymbol{\rho}_1, \boldsymbol{\rho}_2, z)^2 \right] \quad (11)$$

Thus, intensity covariance depends solely on the second-order coherence matrix.

A.9 Correlation Coefficient for Gaussian Fields

Substituting Eq. (11) into Eq. (8) gives

$$b(\rho_d, z) = \frac{\text{Tr} [\mathbf{\Gamma}^{(1,1)}(\boldsymbol{\rho}, -\boldsymbol{\rho}, z)^2]}{\text{Tr} [\mathbf{\Gamma}^{(1,1)}(0, 0, z)^2]} \quad (12)$$

A.10 Contrast (Scintillation Index) for Gaussian Fields

Using Eq. (11) in Eq. (9), the scintillation index becomes

$$c(\boldsymbol{\rho}, z) = \frac{\text{Tr} [\mathbf{\Gamma}^{(4,1)}(\boldsymbol{\rho}, \boldsymbol{\rho}, z)^2]}{\text{Tr} [\mathbf{\Gamma}^{(1,1)}(\boldsymbol{\rho}, \boldsymbol{\rho}, z)]^2} \quad (13)$$

This expression shows that even for Gaussian statistics, intensity fluctuations depend on both coherence and polarization.

B Coherence matrix and propagation

B.1 Beam Coherence–Polarization Matrix and Propagation Law

To describe the spatial coherence and polarization jointly, we employ the beam coherence–polarization (BCP) matrix [2, 5]

$$\overleftrightarrow{\Gamma}_{\alpha\beta}^{(1,1)}(\boldsymbol{\rho}_1, \boldsymbol{\rho}_2, z) = \langle E_\alpha^*(\boldsymbol{\rho}_1, z, t) E_\beta(\boldsymbol{\rho}_2, z, t) \rangle, \quad \alpha, \beta \in \{x, y\}, \quad (23)$$

which reduces to $\mathbf{J}(\boldsymbol{\rho}, z)$ when $\boldsymbol{\rho}_1 = \boldsymbol{\rho}_2 = \boldsymbol{\rho}$. Its propagation in a linear random medium is governed by [5]

$$\overleftrightarrow{\Gamma}^{(1,1)}(\boldsymbol{\rho}_1, \boldsymbol{\rho}_2, z) = \iint \overleftrightarrow{\Gamma}^{(1,1)}(\boldsymbol{\rho}'_1, \boldsymbol{\rho}'_2, 0) K^{(2)}(\boldsymbol{\rho}_1, \boldsymbol{\rho}_2, \boldsymbol{\rho}'_1, \boldsymbol{\rho}'_2; z, k) d^2 \boldsymbol{\rho}'_1 d^2 \boldsymbol{\rho}'_2, \quad (24)$$

where the two-point propagator is the medium-averaged Green's function product

$$K^{(2)} = \langle G^*(\boldsymbol{\rho}_1, \boldsymbol{\rho}'_1; z, k) G(\boldsymbol{\rho}_2, \boldsymbol{\rho}'_2; z, k) \rangle_m. \quad (25)$$

No coupling between orthogonal polarization components occurs in a linear isotropic medium, so the elements of $\overleftrightarrow{\Gamma}^{(1,1)}$ propagate independently and each can be handled within scalar theory.

B.2 Scintillation Index of an Electromagnetic Beam

The instantaneous intensity is

$$I(\boldsymbol{\rho}, z, t) = |E_x|^2 + |E_y|^2, \quad (26)$$

and the scintillation index is defined as [2, 5]

$$\sigma_I^2(\boldsymbol{\rho}, z) = \frac{\langle I^2 \rangle - \langle I \rangle^2}{\langle I \rangle^2}. \quad (27)$$

Writing $I = I_x + I_y$ with $I_x = |E_x|^2$, $I_y = |E_y|^2$, and expanding:

$$\sigma_I^2 = \frac{\sigma_{xx}^2 I_x^2 + 2\sigma_{xy}^2 I_x I_y + \sigma_{yy}^2 I_y^2}{(I_x + I_y)^2}, \quad (28)$$

where the component scintillation indexes are

$$\sigma_{ij}^2 = \frac{\langle I_i I_j \rangle - \langle I_i \rangle \langle I_j \rangle}{\langle I_i \rangle \langle I_j \rangle} = \frac{\Gamma_{ijjj}^{(2,2)} - \Gamma_{ii}^{(1,1)} \Gamma_{jj}^{(1,1)}}{\Gamma_{ii}^{(1,1)} \Gamma_{jj}^{(1,1)}}, \quad i, j \in \{x, y\}. \quad (29)$$

B.2.1 Case A: Fully (Linearly) Polarized Beam

For a beam polarized along x ,

$$\overleftrightarrow{\Gamma}_{(A)}^{(1,1)} = \begin{pmatrix} \Gamma_{xx}^{(1,1)} & 0 \\ 0 & 0 \end{pmatrix}, \quad P_{(A)} \equiv 1. \quad (30)$$

Then $I_y = 0$ and (28) reduces to

$$\sigma_{I,(A)}^2 = \sigma_{xx}^2. \quad (31)$$

B.2.2 Case B: Natural (Unpolarized) Beam

For natural light with mutually independent x - and y -components of equal mean intensities,

$$\overleftrightarrow{\Gamma}_{(B)}^{(1,1)} = \frac{1}{2} \begin{pmatrix} \Gamma_{xx}^{(1,1)} & 0 \\ 0 & \Gamma_{xx}^{(1,1)} \end{pmatrix}, \quad P_{(B)} \equiv 0. \quad (32)$$

Since the components are statistically independent, $\sigma_{xy}^2 = 0$, and (28) gives

$$\sigma_{I,(B)}^2 = \frac{1}{2} \sigma_{xx}^2. \quad (33)$$

B.2.3 Polarization-Based Scintillation Reduction Factor

Comparing (31) and (33), and noting that both beams share the same intensity I and the same degree of coherence (since $\Gamma_{xx}^{(1,1)}$ is identical in the two cases), we obtain the fundamental result [5]

$$\boxed{\sigma_{I,(B)}^2 = \frac{1}{2} \sigma_{I,(A)}^2} \quad (34)$$

for any homogeneous isotropic medium, regardless of turbulence strength.

The purity relation (14) gives an elegant restatement. For a general beam with polarization degree P ,

$$\begin{aligned} \sigma_I^2(\boldsymbol{\rho}, z) &= \frac{\text{Tr}(\boldsymbol{\Omega})}{(\text{Tr} \mathbf{J})^2} - 1 + (\text{spatial coherence terms}) \\ &= \frac{1 + P^2}{2} - 1 + (\text{spatial coherence terms}) \\ &= \frac{P^2 - 1}{2} + (\text{spatial coherence terms}), \end{aligned} \quad (35)$$

making clear that higher polarization increases scintillation: at fixed coherence, the polarization contribution to scintillation is $\propto P^2$.

References

- [1] Vishwakarma, A. and Moosath, K.S., 2025. Distance Measure Based on an Embedding of the Manifold of K-Component Gaussian Mixture Models into the Manifold of Symmetric Positive Definite Matrices. arXiv preprint arXiv:2501.07429.
- [2] Korotkova, O., 2006. Changes in the intensity fluctuations of a class of random electromagnetic beams on propagation. *Journal of Optics A: Pure and Applied Optics*, 8(1), p.30.
- [3] Korotkova, O., 2006. Changes in statistics of the instantaneous Stokes parameters of a quasi-monochromatic electromagnetic beam on propagation. *Optics Communications*, 261(2), pp.218–224.
- [4] Korotkova, O., 2006. Changes in statistics of the instantaneous Stokes parameters of a quasi-monochromatic electromagnetic beam on propagation. *Optics Communications*, 261(2), pp.218–224.
- [5] Korotkova, O., 2008. Scintillation index of a stochastic electromagnetic beam propagating in random media. *Optics Communications*, 281(9), pp.2342–2348.
- [6] Korotkova, O., 2005. Changes in the intensity fluctuations of a class of random electromagnetic beams on propagation. *Journal of Optics A: Pure and Applied Optics*, 8(1), p.30.
- [7] Korotkova, O. and Farwell, N., 2011. Effect of oceanic turbulence on polarization of stochastic beams. *Optics Communications*, 284(7), pp.1740–1746.
- [8] Korotkova, O., Laatikainen, J., Friberg, A. and Setälä, T., 2022. Stokes–Mueller correlation calculus. In *Polarized Light and Optical Angular Momentum for Biomedical Diagnostics 2022* (Vol. 11963, pp. 6–13). SPIE.
- [9] Ata, Y. and Korotkova, O., 2022. Absorption, scattering, and optical turbulence in natural waters. *Applied Optics*, 61(15), pp.4404–4411.
- [10] Laatikainen, J., Friberg, A.T., Korotkova, O. and Setälä, T., 2021. Poincaré sphere of electromagnetic spatial coherence. *Optics Letters*, 46(9), pp.2143–2146.
- [11] Korotkova, O. and Gbur, G., 2021. Jones and Stokes–Mueller analogous calculi for OAM-transforming optics. *Optics Letters*, 46(11), pp.2585–2588.
- [12] De Sande, J.G., Korotkova, O., Santarsiero, M., Martínez-Herrero, R., Piquero, G. and Gori, F., 2022. On-axis polarization of beams radiated by electromagnetic circularly coherent sources. *Optics Letters*, 47(15), pp.3772–3775.
- [13] Yang, Z., Wang, H., Chen, Y., Wang, F., Gbur, G., Korotkova, O. and Cai, Y., 2022. Measurement of the coherence–orbital angular momentum matrix of a partially coherent beam. *Optics Letters*, 47(17), pp.4467–4470.
- [14] Korotkova, O. and Gbur, G., 2021. Unified matrix representation for spin and orbital angular momentum in partially coherent beams. *Physical Review A*, 103(2), p.023529.
- [15] Laatikainen, J., Friberg, A.T., Korotkova, O. and Setälä, T., 2022. Coherence Poincaré sphere of partially polarized optical beams. *Physical Review A*, 105(3), p.033506.
- [16] Abbasirad, N., Barreda, A., Arslan, D., Steinert, M., Fasold, S., Rockstuhl, C., Staude, I., Setzpfandt, F. and Pertsch, T., 2021. Investigation of dipole emission near a dielectric metasurface using a dual-tip scanning near-field optical microscope. *Nanophotonics*, 10(18), pp.4511–4522.
- [17] Scheel, S. and Buhmann, S.Y., 2008. Macroscopic quantum electrodynamics–concepts and applications. *Acta Physica Slovaca*, 58(5), pp.675–809.
- [18] Levine, H. and Schwinger, J., 1950. On the theory of electromagnetic wave diffraction by an aperture in an infinite plane conducting screen. *Communications on Pure and Applied Mathematics*, 3(4), pp.355–391.
- [19] Sipe, J.E. and Van Kranendonk, J., 1974. Macroscopic electromagnetic theory of resonant dielectrics. *Physical Review A*, 9(5), p.1806.

- [20] Poddubny, A.N., Belov, P.A., Ginzburg, P., Zayats, A.V. and Kivshar, Y.S., 2012. Microscopic model of Purcell enhancement in hyperbolic metamaterials. *Physical Review B*, 86(3), p.035148.
- [21] Martin, O.J. and Piller, N.B., 1998. Electromagnetic scattering in polarizable backgrounds. *Physical Review E*, 58(3), p.3909.
- [22] Paulus, M., Gay-Balmaz, P. and Martin, O.J., 2000. Accurate and efficient computation of the Green's tensor for stratified media. *Physical Review E*, 62(4), p.5797.
- [23] Smith, B.C., 2020. Nonlinearity in the Lorentz Oscillator Model. arXiv preprint arXiv:2001.06149.
- [24] Chang, Y.M., Akbari, K., Filipovich, M. and Hughes, S., 2025. Direct space-time modeling of mechanically dressed dipole-dipole interactions with electromagnetically-coupled oscillating dipoles. arXiv preprint arXiv:2505.06514.
- [25] Bowen, P.T., Driscoll, T., Kundtz, N.B. and Smith, D.R., 2012. Using a discrete dipole approximation to predict complete scattering of complicated metamaterials. *New Journal of Physics*, 14(3), p.033038.
- [26] Mirmoosa, M.S., Koutserimpas, T.T., Ptitsyn, G.A., Tretyakov, S.A. and Fleury, R., 2022. Dipole polarizability of time-varying particles. *New Journal of Physics*, 24(6), p.063004.
- [27] Fano, U., 1960. Normal modes of a lattice of oscillators with many resonances and dipolar coupling. *Physical Review*, 118(2), p.451.
- [28] Fisher, W.M. and Rand, S.C., 2010. Light-induced dynamics in the Lorentz oscillator model with magnetic forces. *Physical Review A*, 82(1), p.013802.
- [29] Schelew, E., Ge, R.C., Hughes, S., Pond, J. and Young, J.F., 2017. Self-consistent numerical modeling of radiatively damped Lorentz oscillators. *Physical Review A*, 95(6), p.063853.
- [30] Achouri, K. and Martin, O.J., 2021. Extension of Lorentz reciprocity and Poynting theorems for spatially dispersive media with quadrupolar responses. *Physical Review B*, 104(16), p.165426.
- [31] Golden, K.I., Kalman, G.J., Hartmann, P. and Donkó, Z., 2010. Dynamics of two-dimensional dipole systems. *Physical Review E*, 82(3), p.036402.
- [32] Vugmeister, B.E. and Glinchuk, M.D., 1990. Dipole glass and ferroelectricity in random-site electric dipole systems. *Reviews of Modern Physics*, 62(4), p.993.
- [33] Tamura, M., Wada, T. and Ishihara, H., 2023. Basics of optical force. *Journal of Photochemistry and Photobiology C: Photochemistry Reviews*, 54, p.100570.
- [34] Lembessis, V.E. and Andrews, D.L., 2024. Forces in the Interaction of Light with Matter. *Applied Sciences*, 14(16), p.7008.
- [35] Saif, F. and Watanabe, S., 2023. *Optical Forces on Atoms*. IOP Publishing.
- [36] Zappe, H., 2010. *Fundamentals of Micro-optics*. Cambridge University Press.
- [37] Matsumori, K., Fujimura, R. and Retsch, M., 2023. Electromagnetically Induced Absorption Overcomes the Upper Limit of Light Absorption: Dipole–Dipole Coupling with Phase Retardation in Plasmonic-Dielectric Dimers. *The Journal of Physical Chemistry C*, 127(38), pp.19127–19140.
- [38] Canaguier-Durand, A., Cuche, A., Genet, C. and Ebbesen, T.W., 2013. Force and torque on an electric dipole by spinning light fields. *Physical Review A*, 88(3), p.033831.
- [39] Kumar, P., Kuldinov, D., Castillo, A., Gerakis, A. and Hara, K., 2021. Nonlinear dynamics of coupled light and particle beam propagation. *Physical Review A*, 103(4), p.043502.
- [40] Maiwöger, M., Sonnleitner, M., Zhang, T., Mazets, I., Mallweger, M., Rätzel, D., Borselli, F., Erne, S., Schmiedmayer, J. and Haslinger, P., 2022. Observation of light-induced dipole-dipole forces in ultracold atomic gases. *Physical Review X*, 12(3), p.031018.

- [41] Lu, W., Krasavin, A.V., Lan, S., Zayats, A.V. and Dai, Q., 2024. Gradient-induced long-range optical pulling force based on photonic band gap. *Light: Science & Applications*, 13(1), p.93.
- [42] Castillo, A.M., Kumar, P., Limbach, C.M. and Hara, K., 2022. Mutually guided light and particle beam propagation. *Scientific Reports*, 12(1), p.4810.
- [43] Liu, W. and McLeod, E., 2023. Fast and accurate electromagnetic field calculation for substrate-supported metasurfaces using the discrete dipole approximation. *Nanophotonics*, 12(22), pp.4157–4173.
- [44] Gubskaya, A.V. and Kusalik, P.G., 2002. The total molecular dipole moment for liquid water. *The Journal of Chemical Physics*, 117(11), pp.5290–5302.
- [45] Sain, B., Meier, C. and Zentgraf, T., 2019. Nonlinear optics in all-dielectric nanoantennas and metasurfaces: a review. *Advanced Photonics*, 1(2), pp.024002.
- [46] Xu, S., Sayanskiy, A., Kupriianov, A.S., Tuz, V.R., Kapitanova, P., Sun, H.B., Han, W. and Kivshar, Y.S., 2019. Experimental observation of toroidal dipole modes in all-dielectric metasurfaces. *Advanced Optical Materials*, 7(4), p.1801166.
- [47] Baryshnikova, K.V., Smirnova, D.A., Luk'yanchuk, B.S. and Kivshar, Y.S., 2019. Optical anapoles: concepts and applications. *Advanced Optical Materials*, 7(14), p.1801350.
- [48] Milonni, P.W. and Boyd, R.W., 2010. Momentum of light in a dielectric medium. *Advances in Optics and Photonics*, 2(4), pp.519–553.
- [49] Babicheva, V.E. and Evlyukhin, A.B., 2018. Metasurfaces with electric quadrupole and magnetic dipole resonant coupling. *ACS Photonics*, 5(5), pp.2022–2033.
- [50] Grahm, P., Shevchenko, A. and Kaivola, M., 2012. Electromagnetic multipole theory for optical nanomaterials. *New Journal of Physics*, 14(9), p.093033.
- [51] Akimov, Y.A., 2024. Interaction of light with subwavelength particles: revealing the physics of the electric dipole moment in the classical scattering problem. *Journal of the Optical Society of America B*, 41(9), pp.2114–2121.
- [52] Khlebtsov, B., Melnikov, A., Zharov, V. and Khlebtsov, N., 2006. Absorption and scattering of light by a dimer of metal nanospheres: comparison of dipole and multipole approaches. *Nanotechnology*, 17(5), p.1437.
- [53] Fernandez-Corbaton, I., Nanz, S., Alaei, R. and Rockstuhl, C., 2015. Exact dipolar moments of a localized electric current distribution. *Optics Express*, 23(26), pp.33044–33064.
- [54] Eismann, J.S., Neugebauer, M. and Banzer, P., 2018. Exciting a chiral dipole moment in an achiral nanostructure. *Optica*, 5(8), pp.954–959.
- [55] Weber, W.H. and Ford, G.W., 2004. Propagation of optical excitations by dipolar interactions in metal nanoparticle chains. *Physical Review B*, 70(12), p.125429.
- [56] Terekhov, P.D., Babicheva, V.E., Baryshnikova, K.V., Shalin, A.S., Karabchevsky, A. and Evlyukhin, A.B., 2019. Multipole analysis of dielectric metasurfaces composed of nonspherical nanoparticles and lattice invisibility effect. *Physical Review B*, 99(4), p.045424.
- [57] Lunnemann, P. and Koenderink, A.F., 2016. The local density of optical states of a metasurface. *Scientific Reports*, 6(1), p.20655.
- [58] Naumov, I.I. and Fu, H., 2005. A new method for determining dipole-dipole energy in 1D and 2D systems. *arXiv preprint cond-mat/0505497*.
- [59] Nikitin, A.Y., Garcia-Vidal, F.J. and Martin-Moreno, L., 2012. Analytical expressions for the electromagnetic dyadic Green's function in graphene and thin layers. *IEEE Journal of Selected Topics in Quantum Electronics*, 19(3), pp.4600611.
- [60] Panov, A.V., 2013. Impact of interparticle dipole–dipole interactions on optical nonlinearity of nanocomposites. *Journal of Modern Optics*, 60(11), pp.915–919.

- [61] Panov, A.V., 2010. Contribution of dipolar interactions to third-order nonlinear dielectric susceptibility of nanocomposites. *Optics Letters*, 35(11), pp.1831–1833.
- [62] Sadhukhan, S. and Narayanamurthy, C.S., 2024. Turbulence impacted wavefront corrections using beam modulation technique. *Optics Communications*, p.130716.
- [63] de Magalhaes, A.B., Fonseca, C.D.Á. and Nemes, M.C., 2006. Classical and quantum coupled oscillators: symplectic structure. *Physica Scripta*, 74(4), p.472.
- [64] Rodriguez, S.R.K., 2016. Classical and quantum distinctions between weak and strong coupling. *European Journal of Physics*, 37(2), p.025802.
- [65] Schanz, H. and Esser, B., 1997. Mixed quantum-classical versus full quantum dynamics: Coupled quasiparticle-oscillator system. *Physical Review A*, 55(5), p.3375.
- [66] Novotny, L., 2010. Strong coupling, energy splitting, and level crossings: A classical perspective. *American Journal of Physics*, 78(11), pp.1199–1202.
- [67] Khazanov, T., Gunasekaran, S., George, A., Lomlu, R., Mukherjee, S. and Musser, A.J., 2023. Embrace the darkness: An experimental perspective on organic exciton–polaritons. *Chemical Physics Reviews*, 4(4).
- [68] Yang, W.G. and Schmidt, H., 2021. Acoustic control of magnetism toward energy-efficient applications. *Applied Physics Reviews*, 8(2).
- [69] Canós Valero, A., Bobrovs, V., Weiss, T., Gao, L., Shalin, A.S. and Kivshar, Y., 2024. Bianisotropic exceptional points in an isolated dielectric nanoparticle. *Physical Review Research*, 6(1), p.013053.
- [70] Berk, C., Jaris, M., Yang, W., Dhuey, S., Cabrini, S. and Schmidt, H., 2019. Strongly coupled magnon–phonon dynamics in a single nanomagnet. *Nature Communications*, 10(1), p.2652.
- [71] Deng, Z.L., Li, F.J., Li, H., Li, X. and Alu, A., 2022. Extreme diffraction control in metagratings leveraging bound states in the continuum and exceptional points. *Laser & Photonics Reviews*, 16(6), p.2100617.
- [72] Godejohann, F., Scherbakov, A.V., Kukhtaruk, S.M., Poddubny, A.N., Yaremkevich, D.D., Wang, M., Nadzeyka, A., Yakovlev, D.R., Rushforth, A.W., Akimov, A.V. and Bayer, M., 2020. Magnon polaron formed by selectively coupled coherent magnon and phonon modes of a surface patterned ferromagnet. *Physical Review B*, 102(14), p.144438.
- [73] Passler, N.C., Gubbin, C.R., Folland, T.G., Razdolski, I., Katzer, D.S., Storm, D.F., Wolf, M., De Liberato, S., Caldwell, J.D. and Paarmann, A., 2018. Strong coupling of epsilon-near-zero phonon polaritons in polar dielectric heterostructures. *Nano Letters*, 18(7), pp.4285–4292.
- [74] Genco, A., Louca, C., Cruciano, C., Song, K.W., Trovatiello, C., Di Blasio, G., Sansone, G., Randerson, S.A., Claronino, P., Georgiou, K. and Jayaprakash, R., 2025. Femtosecond switching of strong light-matter interactions in microcavities with two-dimensional semiconductors. *Nature Communications*, 16(1), p.6490.
- [75] Peters, K.J. and Rodriguez, S.R., 2022. Exceptional precision of a nonlinear optical sensor at a square-root singularity. *Physical Review Letters*, 129(1), p.013901.